Article:
Morrison, K. orcid.org/0000-0001-5672-3310, Betouras, J.J., Venkat, G. orcid.org/0000-0001-6255-3151 et al. (5 more authors) (2024) Emergence of a hidden magnetic phase in LaFe11.8Si1.2 investigated by inelastic neutron scattering as a function of magnetic field and temperature. Advanced Physics Research. 2400008. ISSN 2751-1200

https://doi.org/10.1002/apxr.202400008

ADVANCED PHYSICS RESEARCH Open Access
www.advphysicsres.com

Emergence of a Hidden Magnetic Phase in $LaFe_{11.8}Si_{1.2}$ Investigated by Inelastic Neutron Scattering as a Function of Magnetic Field and Temperature

Kelly Morrison, Joseph J. Betouras, Guru Venkat, Russell A. Ewings, Andrew J. Caruana, Konstantin P. Skokov, Oliver Gutfleisch, and Lesley F. Cohen*

The $NaZn_{13}$ type itinerant magnet $LaFe_{13-x}Si_x$ has seen considerable interest due to its unique combination of large magnetocaloric effect and low hysteresis. Here, this alloy with a combination of magnetometry, bespoke microcalorimetry, and inelastic neutron scattering is investigated. Inelastic neutron scattering reveals the presence of broad quasielastic scattering that persists across the magnetic transition, which is attributed to spin fluctuations. In addition, a quasielastic peak is observed at $Q = 0.52$ Å^{-1} for $x = 1.2$ that exists only in the paramagnetic state in proximity to the itinerant metamagnetic transition and argue that this indicates emergence of a hidden mag the netic phase that drives the first-order phase transition in this system.

1. Introduction

The application of magnetic materials for magnetic cooling (magnetocaloric effect) was initiated over 20 years ago by the discovery of large magnetic entropy changes in the magnetostructurally coupled $Gd_5Ge_2Si_2$.[1] Since then, exploration has yielded several material systems[2] and expanded the application of the magnetocaloric effect to areas such as local hyperthermia for medical applications,[3] and thermal energy harvesting.[4]

One of the key requirements for widespread application of magnetocaloric materials in magnetic refrigeration is a material with large adiabatic temperature changes that can be repeatedly cycled in field and temperature. While several material systems have been investigated, it is primarily the itinerant ferromagnets $LaFe_{13-x}Si_x$ and $Mn_xFe_{1.95-x}P_{1-y}Si_y$,[5,6] that have emerged as the most promising materials for application close to room temperature. These materials share the property of strong coupling between lattice and spin degrees of freedom, large entropy changes, relatively small energy losses due to hysteresis, and tunability by chemical substitution. A thorough understanding of the emergent behavior due to the interconnection of the different degrees of freedom in these materials, is highly desirable in order to be able to predict new material systems[7] and to use them efficiently in emerging technologies. In the present work, we reveal and analyze new aspects of the magnetic properties of the $LaFe_{13-x}Si_x$ system, which plays a key role in driving the first-order phase transition.

For $x = 1.6$, $LaFe_{13-x}Si_x$ (LFS) has a first-order ferromagnetic (FM), to paramagnetic (PM), transition that is tunable in magnetic field, ending at a tricritical point (H_{crit}, T_{crit}) beyond which it is a second order phase transition.[8,9] In this large family of materials the magnetic phase transition can be easily tailored by changing the Fe content,[10] hydrogenation, or by substitution of Fe for other magnetic transition metals (Mn, Co).[11] LFS is promising as it exhibits a strong, first-order magneto- volume phase transition,[5] with large associated entropy and adiabatic temperature changes, and crucially, once extrinsic contributions are accounted for there is almost no magnetic or thermal hysteresis,[12] which is an advantage for cooling applications. This was demonstrated previously using microcalorimetry by comparing the entropy change due to latent heat to magnetic hysteresis of various other magnetocaloric materials.[13]

Kuz'min and Richter put forward an explanation for the low hysteresis observed in LFS in terms of a free energy landscape of

K. Morrison, J. J. Betouras
Department of Physics and Centre for the Science of Materials
Loughborough University
Loughborough LE11 3TU, UK
E-mail: k.morrison@lboro.ac.uk
G. Venkat
Department of Materials Science and Engineering
University of Sheffield
Sheffield S1 3JD, UK
R. A. Ewings, A. J. Caruana
ISIS Pulsed Neutron and Muon Source
STFC Rutherford Appleton Laboratory
Harwell Campus, Didcot, Oxon OX11 0QX, UK
K. P. Skokov, O. Gutfleisch
Institute of Materials Science
Functional Materials
Technical University Darmstadt
64287 Darmstadt, Germany
L. F. Cohen
The Blackett Laboratory
Imperial College London
South Kensington Campus, London SW7 2AZ, UK

The ORCID identification number(s) for the author(s) of this article can be found under https://doi.org/10.1002/apxr.202400008

DOI: 10.1002/apxr.202400008

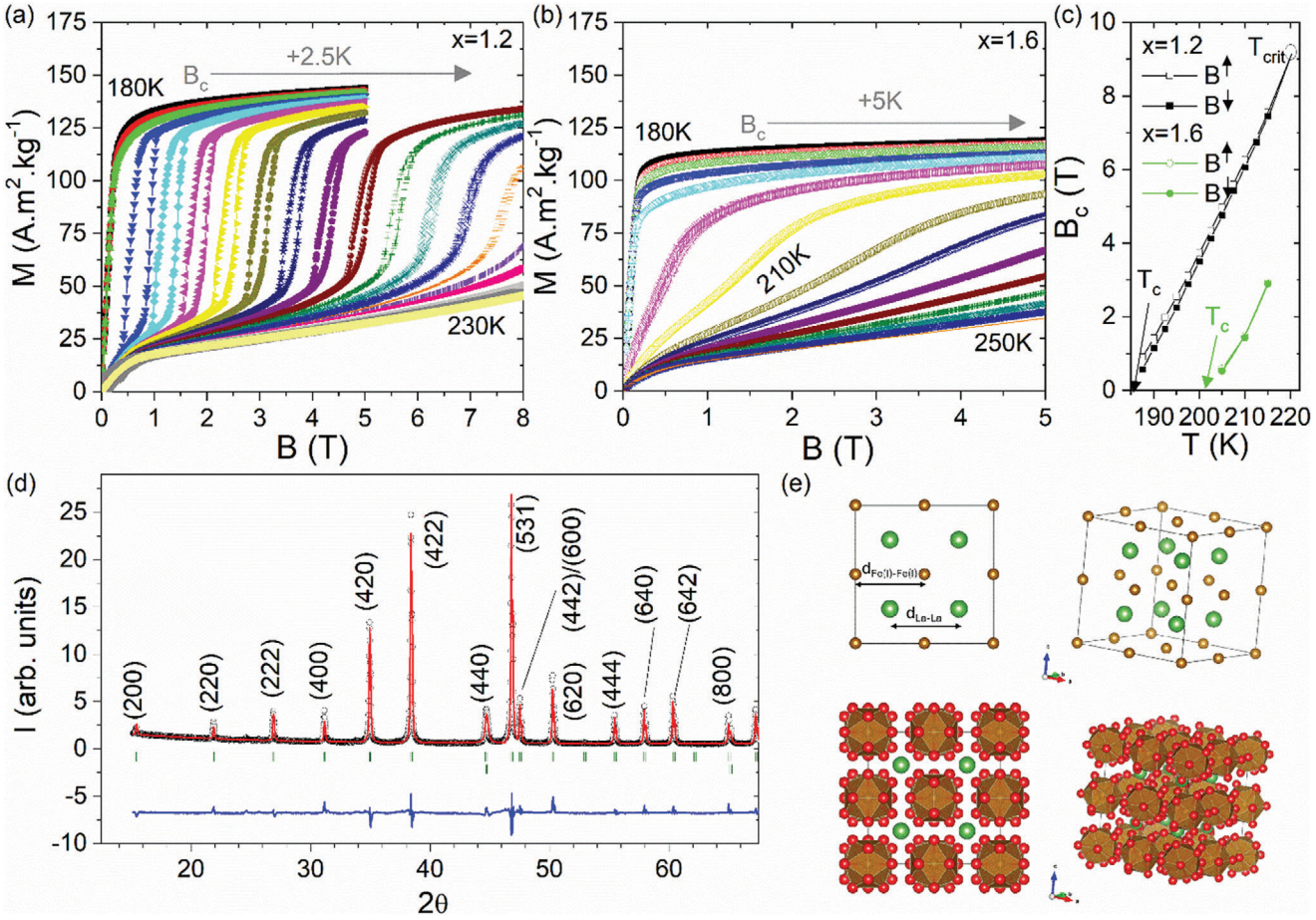

Figure 1. Summary of magnetization data for $LaFe_{13-x}Si_x$ for a) $x = 1.2$, and b) $x = 1.6$ at different temperatures. As the silicon content, x, is increased (or the temperature increased) the field driven phase transition broadens with an associated decrease in hysteresis. c) Magnetic phase diagram for each sample, where $B^{\uparrow}$ is the field at which the magnetization has jumped to 50% of its saturation value from the paramagnetic state, and $B^{\downarrow}$ is the point at which it falls to 50% of saturation value from its ferromagnetic state. Arrows indicate the Curie temperature, T_c, for each sample. d) Indexed x-ray diffraction data for $x = 1.2$. The first observable Bragg peak was the (200) at $2\theta = 15.5$ °. e) Schematic of the crystal structure. Top: *8a* and *8b* sites showing position of the Fe_I and La atoms. Bottom: full structure showing the icosahedral clusters of Fe_{II} that surround each Fe_I atom.

several local minima associated with different spin states, separated by low energy barriers.[14] It has also been argued that the reduced hysteresis is a consequence of spin fluctuations (SFs) lowering (renormalizing) the energy barriers one might normally expect of a first-order phase transition.[15,16] More recently, evidence has started to emerge of paramagnetic (PM) SFs in LFS[17–19] but a full understanding remains incomplete. In this work we present inelastic neutron scattering (INS) data for $x = 1.2$ and 1.6 above and below the Curie temperature, T_c, and find that quasielastic excitations, which we attribute to SFs, appear in the PM state, persisting to higher temperatures. In addition, we observe the emergence of a finite Q peak at 0.52 Å^{-1} in $x = 1.2$ that disappears as T_{crit} is approached and the latent heat approaches zero. We argue that this suggests presence of a hidden phase that drives the first-order phase transition.

2. Results

Figure 1 shows magnetometry data for the samples presented here ($x = 1.2$, 1.6), which follows the classic itinerant metamagnetic behavior reported previously: an s-shaped curve, which broadens as the applied magnetic field is increased, with a corresponding decrease in magnetic hysteresis.[13,15] The magnetic phase diagrams determined for these samples are also shown in Figure 1c, where the Curie temperature for each sample is indicated, and the tri-critical point (T_{crit}) could be estimated from the point at which hysteresis approaches zero, which is approximately 220 K for $x = 1.2$.

Room temperature XRD of the $x = 1.2$ sample, shown in Figure 1d, confirmed a majority phase of $LaFe_{11.8}Si_{1.2}$ (89.9%) with $NaZn_{13}$ type *Fm*-3*c* space group and lattice parameter 11.474 Å alongside a secondary phase of α-Fe (10.1%, space group *Im*-3*m*, $a = 2.8648$ Å), which is common for this system.[11] We also show in Figure 1e the crystal structure of the $LaFe_{11.8}Si_{1.2}$ phase, where La atoms occupy the *8a* site, Fe_I the *8b* site (shown in the top half of Figure 1e) and Fe_{II} atoms occupy the *96i* site. High-resolution neutron diffraction has previously shown that the Si atoms preferentially substitute on the Fe_{II} (*96i*) site[20] and that the addition of Si both stabilizes the $La(Fe,Si)_{13}$ phase as well as drives the magnetic phase transition from first order to second

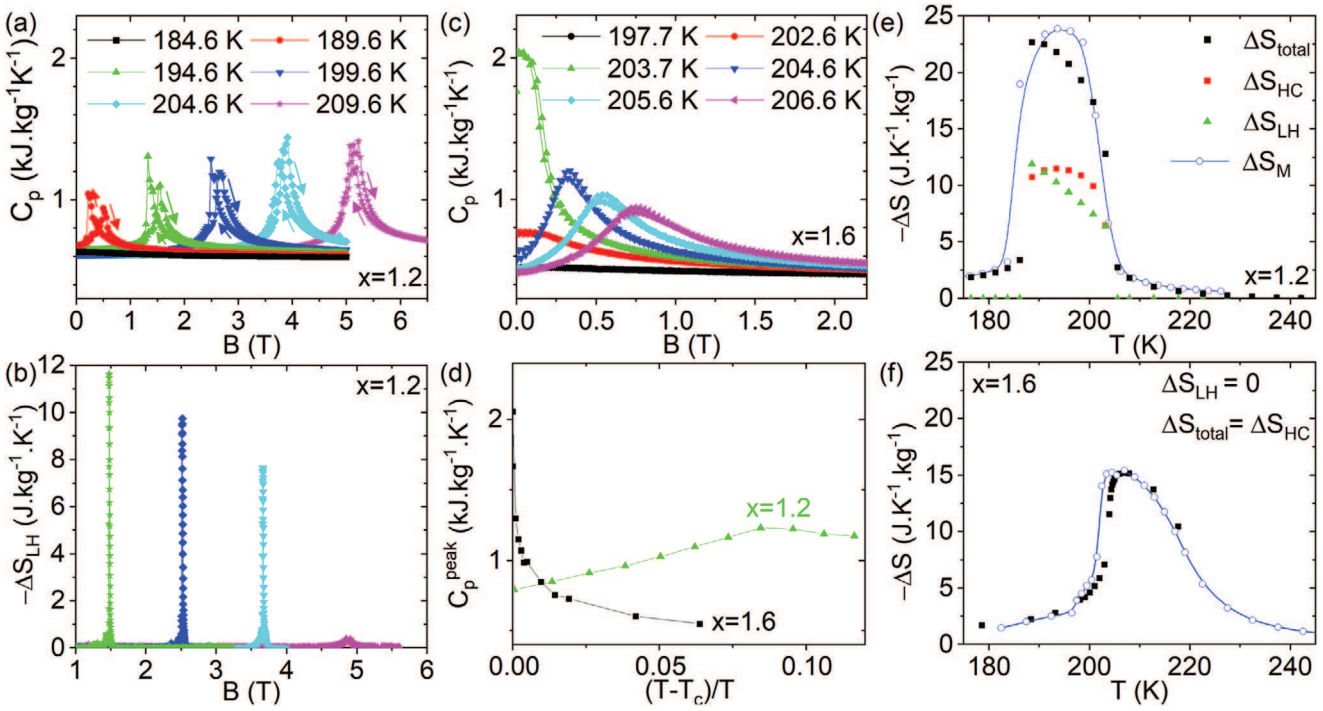

Figure 2. Summary of microcalorimetry measurements and calculated entropy change for $\Delta B = 0$–4 T. a) AC heat capacity for $x = 1.2$ ($T_c = 186$ K) and b) the corresponding entropy change measured due to latent heat, ΔS_{LH}. c) AC heat capacity for $x = 1.6$ ($T_c = 204$ K); no latent heat was observed. d) Summary of the maximum observed AC heat capacity as a function of reduced temperature, demonstrating that it peaks further away from T_c as the phase transition becomes more first order. e) Calculated entropy change from magnetometry (ΔS_M), AC heat capacity (ΔS_{HC}), latent heat measurements (ΔS_{LH}) and total ($\Delta S_{total} = \Delta S_{HC} + \Delta S_{LH}$) for $x = 1.2$. f) Calculated entropy change for $x = 1.6$.

order. These Fe_{II}/Si atoms form icosahedral clusters about the Fe_I atoms.

Figure 2 presents a summary of microcalorimetry data for $x = 1.2$ and 1.6, where AC heat capacity, C_p (Figure 2a,c), exhibited a field-driven peak, as summarized in Figure 2d. This peak in C_p is maximum for $x = 1.6$ at $B = 0$ T, where the phase transition is second order, as confirmed by lack of measurable latent heat or magnetic hysteresis in Figure 1b,c. The field-driven entropy change corresponding to the AC heat capacity can be determined using Equation 1, where ΔC_p is the field-driven change in heat capacity, and T is the temperature. The corresponding entropy change due to latent heat, ΔS_{LH} can be determined using Equation 2, where ΔQ is the measured (field driven) heat output in J kg^{-1}.

$$\Delta S_{HC} = \int_0^T \frac{\Delta C_p}{T}\, dT \tag{1}$$

$$\Delta S_{LH} = \frac{\Delta Q}{T} \tag{2}$$

Figure 2b shows ΔS_{LH} measured for $x = 1.2$, where it can be seen that it decreased as the temperature (and thus field required to drive the phase transition) was increased. The combined entropy change calculated from magnetometry (ΔS_M) and these thermal measurements ($\Delta S_{total} = \Delta S_{HC} + \Delta S_{LH}$) is shown in Figure 2e,f. There is documented general agreement between the two methods despite comparing different sized samples,[21] however it is useful to note that: 1) slight differences are expected due to the difference in quantity of material measured, and 2) while the latent heat contribution to entropy change, ΔS_{LH}, decreased, the heat capacity contribution, ΔS_{HC}, remained roughly constant.

The observed decrease in ΔS_{LH} as the temperature was increased was previously attributed to approaching T_{crit}, above which the phase transition is second order.[22] We can therefore determine T_{crit} from microcalorimetry data by extrapolating the point at which ΔS_{LH} approaches zero. Assuming that it decreased linearly with increasing temperature, it can be determined as $T_{crit}(x = 1.2) = 221 \pm 1$ K, which is in agreement with magnetometry data. In contrast, as ΔS_{LH} decreased, approaching zero at T_{crit}, the features observed in the AC heat capacity measurements initially increased in magnitude, reaching in excess of 200% of $C_p(B = 0$ T, $T > T_c)$, before decreasing again, as summarized in Figure 2d.

INS was used as a tool here to measure the emergence of SFs about T_c that were theorized to be the source of enhancement observed in heat capacity measurements, as well as renormalization of the energy barrier (and thus the lower observed magnetic hysteresis). It should be noted that whilst previous measurements[18,19,23,24] indicated presence of SFs for $Q \leq 0.8$ $Å^{-1}$ and a phonon peak near 27 meV in the FM state, they did not have the low Q resolution (to 0.1 $Å^{-1}$) as well as magnetic field dependence presented here. Zhang et al. reported observation of magnetic diffuse scattering for $x = 1.4$, and an additional peak at $Q = 0.5$ $Å^{-1}$ that they attributed to fast FM fluctuations,[19]

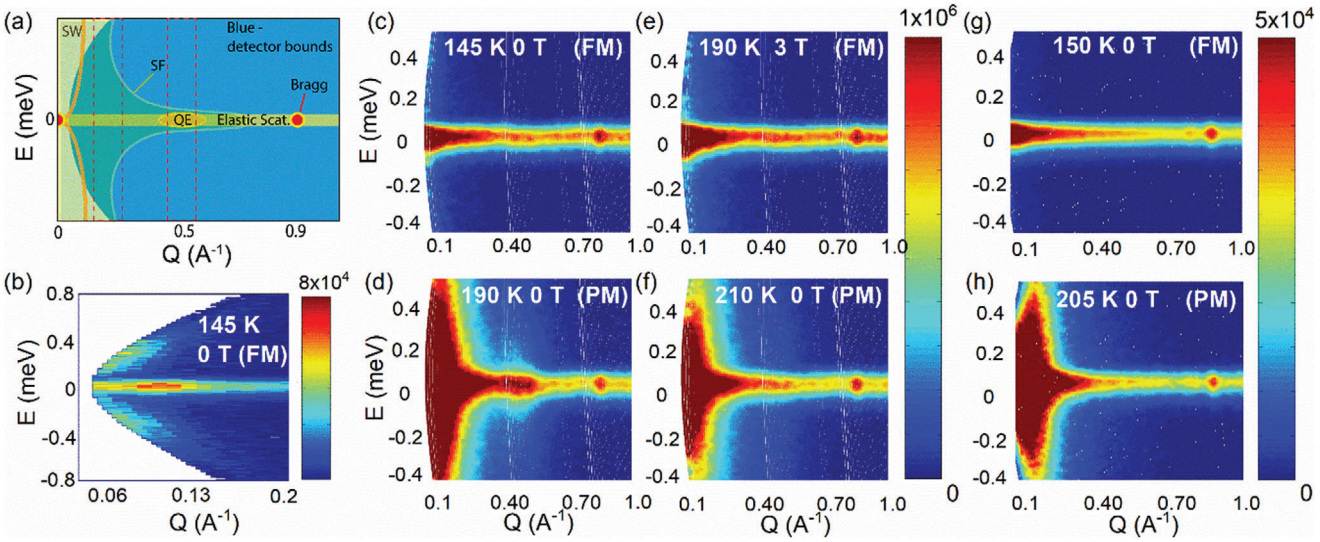

Figure 3. a) Schematic of the contributions to the observed polycrystalline inelastic neutron scattering: spin waves (SWs), spin fluctuations (SFs), finite-Q quasielastic feature (QE), Elastic scattering and Bragg peaks. The blue area indicates the E–Q space observable at a given incident energy, E_i. b–f) Examples of INS $E(Q)$ maps obtained for $x = 1.2$ on LET as a function of temperature and applied magnetic field, where $E_i = 3.6$ meV. b,c) Below T_c, the sample is in the FM phase, where signature of a SW is observable close to b) the edge of the detector bounds and c) no quasielastic features are present. d) Above T_c, giant fluctuations appear about the elastic line from $Q = 0$ Å^{-1} to approximately 0.7 Å^{-1} (SFs) as well as an additional feature at $Q \approx 0.52$ Å^{-1} (QE). e) As the magnetic field is increased and the magnetic phase driven from PM to FM, the SFs seen in (d) are suppressed. f) Close to the tri-critical point, T_{crit} (above which the field driven phase transition is second order), enhanced quasielastic scattering is still present (SFs) but heavily suppressed and the QE feature is less evident. g,h) Examples of INS maps obtained for $x = 1.6$ on LET as a function of temperature, where $E_i = 3.6$ meV. g) Below T_c, the behavior is similar to $x = 1.2$. h) Just above T_c, SFs are observed, but with no corresponding QE feature. (Color scale indicates intensity, $I(Q,E)$ on a linear scale.).

however this was for relatively large temperature intervals and at zero magnetic field.

Initial measurements of $x = 1.2$ performed on the MARI beamline showed evidence of a peak in quasielastic scattering close to the zeroth order peak at $Q = 0$ Å^{-1}, with a maximum around T_c. The intensity of this feature persisted for more than 10 K above T_c (i.e., well into the paramagnetic state) and dropped off rapidly as the sample approached T_{crit} (see Figure S1 in Supporting Information). Example $E(Q)$ scans from higher resolution INS obtained on the LET beamline using a primary energy, E_i, of 3.6 meV are summarized in **Figure 3**, where Figure 3a gives a general schematic of the features observed and Figure 3b–h show example $E(Q)$ maps above and below T_c ($T_c = 186$ K for $x = 1.2$, 204 K for $x = 1.6$), where it is indicated whether the sample was in a ferromagnetic (FM) or paramagnetic (PM) phase. In general, there were several key features that were observed, which were summarized in the schematic of Figure 3a. For $x = 1.2$ this included:

1) An elastic scattering line at $E = 0$ meV, with the zeroth order peak at $Q = 0$ Å^{-1}, the (200) Bragg reflection for LFS at $Q = 1.095$ Å^{-1}, and a minor unidentified Bragg reflection at $Q = 0.86$ Å^{-1} (see Figure S2, Supporting Information).
2) Observable spin waves (SWs) emerging from the zeroth order peak and (200) Bragg reflection when $T < T_c$ (see Figure S3, Supporting Information).
3) Quasielastic scattering across the range $0 < Q < 0.7$ Å^{-1} when $T > T_c$, that we attribute to spin fluctuations (SFs).
4) A finite-Q quasielastic peak at 0.52 Å^{-1} (QE), when $T_c < T < T_{crit}$.

We also show example $E(Q)$ maps obtained from zero field measurements of $x = 1.6$, which, as discussed earlier, exhibited a second-order phase transition. In this case, whilst SFs were observed above T_c, there was no indication of a finite-Q feature (QE) (Figure 3g,h).

To summarize, for the $x = 1.2$ and 1.6 samples below T_c, the sample would have been fully in the FM state (Figure 3b,c,e,g). Here we saw the convolution of the tail of the zeroth order peak with the elastic line at $E = 0$ meV. Just above T_c (Figure 3d,h for $x = 1.2$ and 1.6, respectively), the sample was in the PM state and giant fluctuations that we attribute to SFs were observed. Note that this was accompanied by a finite-Q feature at 0.52 Å^{-1} (QE) in the $x = 1.2$ sample only. As a magnetic field of 3 T was applied to the $x = 1.2$ sample at $T = 190$ K, it collapsed into the FM state: SFs and QE features disappeared (Figure 3e). Closer to T_{crit} (= 221 K for $x = 1.2$), as seen in Figure 3f, the intensity of the SF feature appears to have decreased, as has the QE feature. Overall, this shows the emergence of quasielastic scattering in the PM state, out to approximately 0.7 Å^{-1}, in addition to a finite-Q QE feature for $x = 1.2$ at 190 K and 210 K and $B = 0$ T (PM state), but not for $x = 1.2$ at 190 K for 3 T (FM state) or $x = 1.6$.

Multiple datasets were obtained about the field driven magnetic phase transition for $x = 1.2$, as summarized by the onset field phase diagram of **Figure** 4a. This phase diagram shows the range of onset fields, B_{start} and B_{end}, which were determined from magnetometry. They were defined as the point at which 10% and 90% of the saturation magnetization, M_{sat}, was reached. As this phase transition is very sensitive to temperature and magnetic field, we also determined the point at which the field-driven phase transition had occurred during neutron scattering

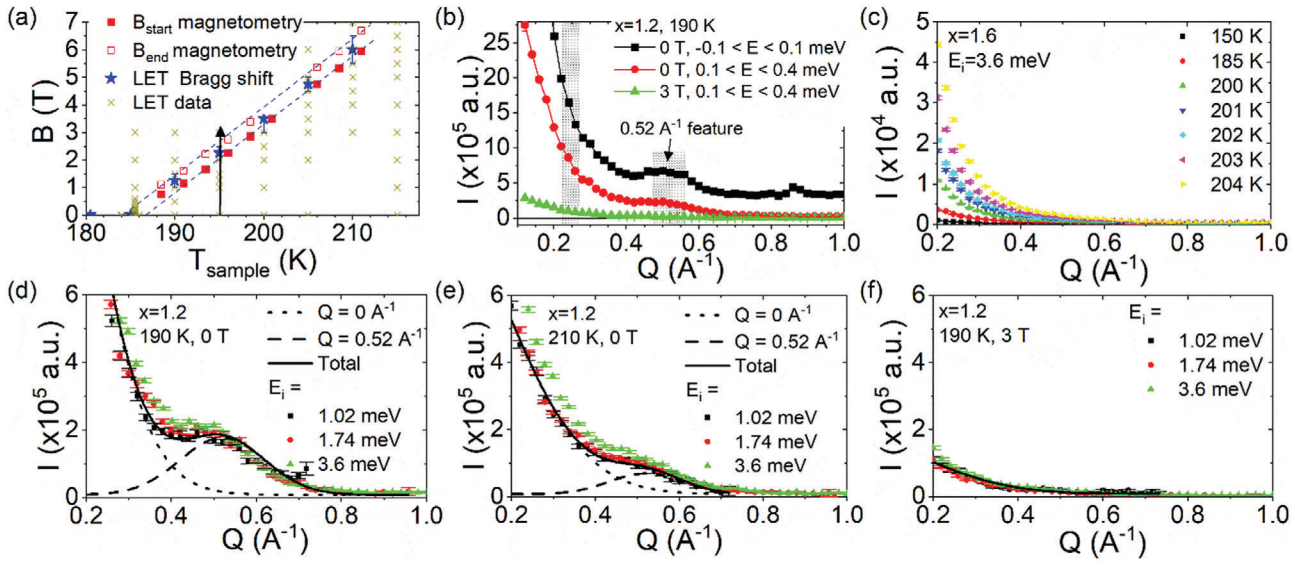

Figure 4. a) Onset field phase diagram determined by magnetometry (red symbols) and shift in the (200) Bragg peak at the elastic line (star symbols). The arrow indicates the field history of a measurement, where the magnetic state was reset at $B = 0$ T by heating above T_c and cooling to the chosen measurement temperature. Each available LET dataset is indicated by the cross symbols. b) Example linescans just above T_c integrated about -0.1 meV $< E <$ 0.1 meV and 0.1 meV $< E <$ 0.4 meV. The hashed areas indicate the integration window used to isolate SF and QE features; a.u. is used as shorthand for "arbitrary units." c) Corresponding linescan for $x = 1.6$, $E_i = 3.6$ meV, where no QE feature was observed and intensity due to SFs increases as T_c of 204 K is approached. d–f) Example of the QE feature observed at $E_i = 1.02$, 1.74, 3.6 meV for $x = 1.2$ at d) 190 K, 0 T; e) 190 K, 3 T; and f) 210 K, 0 T. For comparison, the same integration range was used for each linescan in (c–f) of $0.1 < E < 0.4$ meV and an example fit of the {SF + zeroth order peak} at $Q = 0$ Å^{-1}, and QE feature at $Q = 0.52$ Å^{-1} is given for (d,e) where it was observed.

measurements by observing the shift in the (200) Bragg reflection due to the 1.5% volume change associated with this phase transition. This is shown by the blue star markers that fall within the range of onset fields determined from magnetometry (equivalent to a 3 K range in T_c for individual fragments).

For each set of INS measurements at a given temperature the magnetic state was first "reset" by warming the sample in zero field above 195 K. Data was then collected as the magnetic field was increased, examples of which were shown in Figure 3. Figure 4b shows example line scans with respect to Q that were obtained by integrating the intensity, $I(Q,E)$, between $-0.1 \leq E \leq 0.1$ meV (elastic line) and $0.1 \leq E \leq 0.4$ meV (quasielastic region). Close to T_c, two distinct features were observed in both: the first which we attribute to SFs for $Q < 0.7$ Å^{-1}; and a second finite Q peak in the range $0.48 < Q < 0.56$ Å^{-1}. This demonstrates the presence of diffuse quasielastic scattering away from the elastic line (with decreasing intensity).

In Figure 4d–f, we show examples of linescans determined using the quasielastic integration range $0.1 \leq E \leq 0.4$ meV at temperatures and magnetic field equivalent to those shown in Figure 3 for $x = 1.2$. We also show in Figure 4c these linescans for $x = 1.6$, $E_i = 3.6$ meV as T was increased above T_c. While no QE feature was observed, it is clear that the intensity of the inelastic scattering due to SFs increased as T_c was approached.

To chart the evolution of the SFs and QE peak as a function of magnetic field and temperature we fit this data to obtain the integrated intensity, S, across a fixed range of Q. For each measurement in $x = 1.2$ where SFs were observed, we extracted the corresponding linescan with respect to E in the region $0.15 < Q <$ 0.25 Å^{-1}. We chose this range as it was far enough away from the QE feature to consider its contribution negligible and for the chosen E_i there were enough points in $E(Q)$ space to integrate over. A pseudoVoigt function was fit to each linescan, where the Gaussian function was representative of the incoherent background of the elastic line with a constant FWHM of 0.11 meV. A representative fit is given in **Figure 5a**, where the high field (3T) data is shown alongside the Gaussian fit, $G(E)$, to demonstrate how well it fits to the remaining elastic line when the intensity of SF scattering decreases to zero in the FM state. The inset shows the obtained linewidth as a function of applied magnetic field, B. The integrated intensity obtained from these fits is given in Figure 5b. As the temperature was increased the uncertainty increased due to broadening of the SF peak and the limited range of datapoints in E for this E_i and Q range (due to detector bounds indicated in the sketch of Figure 3a). In general, it is clear that as B increased so did the intensity of the SF scattering and the lifetime (i.e., linewidth of the fitted peak). This mirrors the behavior seen in heat capacity data of Figure 2: an increase in heat capacity as you approach the phase transition (B,T) with increasing temperature, even as the latent heat decreases.

With regards to the QE feature at $Q = 0.52$ Å^{-1}, we chose the region $0.48 < Q < 0.56$ Å^{-1} to integrate over to produce similar linescans to Figure 5a. In this case, however, the contribution due to SFs needs to be considered as it does vary noticeably with field and temperature within this Q range. Due to detector bounds, the $E(Q)$ space that was sampled will not cover the zeroth order peak, which makes it difficult to separate background contributions due to this from the SFs when examining the QE feature in this range. Therefore, to isolate the amplitude of the QE feature, we first determined the $I(T, Q, E, B)$ dependence of the SF contribution at $Q = 0.52$ Å^{-1}. This was achieved by fitting the integrated Q linescans (similar to that seen in Figure 4) for integration

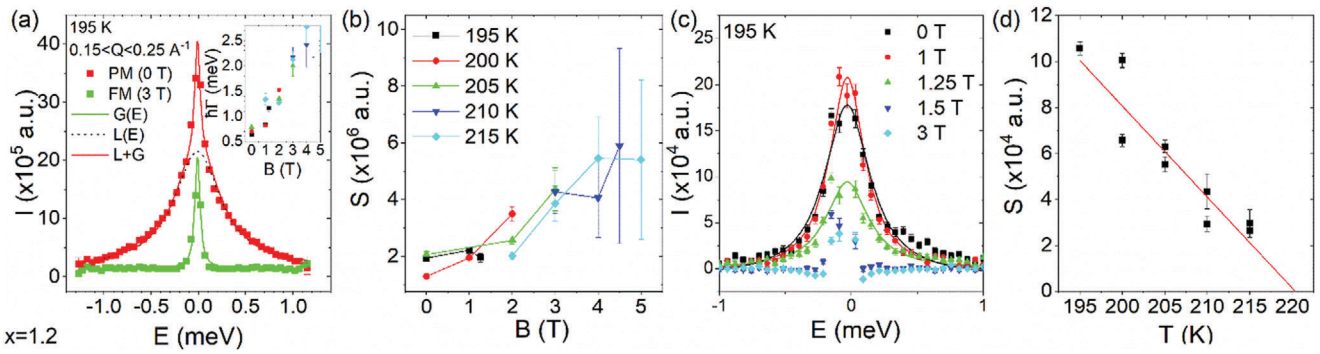

Figure 5. Summary of analysis of INS data obtained on LET, for $E_i = 3.6$ meV. a) Example linescans in the PM (0 T) and FM (3 T) state for 0.15 Å^{-1} < Q < 0.25 Å^{-1}, alongside the pseudoVoigt used to determine linewidth shown in inset and integrated intensity, S, shown in (b). c) Example linescan for 0.48 Å^{-1} < Q < 0.56 Å^{-1} after background removal detailed in text. d) Corresponding integrated intensity, S, determined from fitting 0.48 Å^{-1} < Q < 0.56 Å^{-1} linescans at different temperature and fields where the QE feature was present.

intervals of 0.03 meV to a Lorentzian centered at $Q = 0$ Å^{-1}, with the QE feature and any Bragg reflections masked (Q = 0.4–0.6 Å^{-1} and >0.8 Å^{-1}). These fits were then used to determine the background contribution due to SFs at $Q = 0.52$ Å^{-1} and subtracted from the QE linescans, an example of which is given in Figure 5c. Fitting a Lorentzian function to this data resulted in a lifetime of 1.52 ± 0.6 ps and an integrated intensity that appears to decrease linearly with temperature (Figure 5d). Linear extrapolation of this trend suggests that it would reach zero at $T = 220$ K, which is within error of the tri-critical temperature determined from microcalorimetry of $T_{crit} = 221 \pm 1$ K. We note that whilst this feature is close to the position of the (100) Bragg peak (Q = 0.54 Å^{-1}), this is a forbidden reflection for this system and is still far enough away that other factors should be properly considered.

3. Discussion

In order to explain the observation of strong magnetic fluctuations peaked at finite Q, we considered two phenomenological paths. The first was associated with the magnetic fluctuations that occur with the development of the FM moment. In this case the total magnetization is written as $M_{tot} = M + m_{||} + m_{\perp}$, where M is the ferromagnetic part, $m_{||}$ the longitudinal fluctuations and $m_{\perp}$ the transverse fluctuations. The ferromagnetic part can be taken to be along the z-axis, without loss of generality. The minimal Ginzburg-Landau (GL) free energy functional of the system is:

$$\mathcal{F} = \int d^3x \left[\alpha M_{tot}^2 + \beta M_{tot}^4 + \gamma M_{tot}^6 + \delta\left(\nabla M_{tot}\right)^2 + \epsilon\left(\nabla^2 M_{tot}\right)^2\right] \quad (3)$$

The underlying assumption regarding fluctuations is that although their spatial average is zero, this is not the case for $<m_i^2>$ with i = ⊥, ||. As there is no developed long-range order, we keep terms up to second order in m_i but it is essential to retain the next higher order in derivatives. The Fourier transform of the part of the fluctuations in the free energy for $T > T_c$ is:

$$\mathcal{F}_{fl} = \int \frac{d^3q}{(2\pi)^3} \chi^{-1}(q) \left[m_{||}(q)\, m_{||}(-q) + m_{\perp}(q)\, m_{\perp}(q-)\right] \quad (4)$$

with $\chi^{-1}(q) = \delta q^2 + \epsilon q^4 + \alpha$. If $\delta < 0$ then $\chi(q)$ is peaked at a finite value of $Q = \sqrt{-\frac{\delta}{2\epsilon}}$. This value is not very sensitive to the value of magnetization M. Both transverse and longitudinal fluctuations need to be retained because the peak is seen in the regime where $M = 0$ ($T > T_c$) and drops significantly below T_c where the terms proportional to M^2 and M^4 are added to $\chi^{-1}(q)$. On the other hand, for the argument to be sound we need to retain a positive susceptibility $\chi(q)$ at all temperatures. This constrains the value of $\delta^2/2\epsilon$ to be always less than α for $T > T_c$, and as a result the value of Q should carry a strong temperature-dependence and should decrease to 0 as the temperature approaches T_c. As we did not observe a Q dependence of the finite feature, we expect another source is responsible.

The alternative scenario that appears physically reasonable is that two different phases compete: the pure FM phase and a magnetic (possibly antiferromagnetic or ferrimagnetic) phase of finite-Q. The parts of the free energy in the Ginzburg Landau functional for each order parameter are independent (with a possible mixing term which does not change the physics qualitatively). In the data, the onset of the winning order parameter at T_c is clearly seen, while the second competing phase demonstrates itself only through the observed finite-Q (QE) fluctuations (Figures 3 and 4b,d,e), where the material exhibits a first-order phase transition. These fluctuations are intense in the disordered region, where the phases compete, while they are much weaker below T_c, as the prevailing state has already emerged.

We argue that it is likely that the competing magnetic phase is antiferromagnetic order as this has been observed in an analogue system—$LaFe_{11.4}Al_{1.6-x}Si_x$—where it was shown previously that the addition of Si drives magnetic exchange from AFM to FM.[25,26] One possible cause of this could be a variation in RKKY exchange between the Fe_I and Fe_{II} ions of the unit cell as their separation is modified. As high-resolution neutron diffraction has shown that the Si atoms preferentially substitute on the Fe_{II} (*96i*) site,[30] the addition of smaller Si atoms will distort the icosahedral clusters seen in Figure 1e and modify Fe_I–Fe_I, Fe_{II}–Fe_{II}, and Fe_I–Fe_{II} distances. Given the observation of the QE feature for $x = 1.2$ (lowest Si concentration with stable phase), that is not present for $x = 1.6$ (where the phase transition is now second order) we hypothesize that the Si doping modifies the RKKY

exchange enough to lock out the emergence of an AFM phase. In addition, we note that the observed QE for $x = 1.4$ at $Q = 0.5$ Å^{-1},[19] and $x = 1.2$ at $Q = 0.52$ Å^{-1} [this work] seem to indicate that we are approaching commensurate AFM ordering as Si content, x, is decreased by approaching the forbidden crystallographic (100) Bragg reflection at $Q = 0.54$ Å^{-1}.

4. Conclusion

To summarize, in this letter we present for the first time, high-resolution INS measurement of the $LaFe_{11.8}Si_{1.2}$ intermetallic as a function of temperature and applied magnetic field. We show emergence of diffuse scattering above T_c, which is accompanied by a finite-Q peak at 0.52 Å^{-1}. As LFS is driven towards a second order phase transition (whether by addition of Si, or increasing temperature and applied magnetic field), the diffuse scattering due to SFs remain, whilst this finite-Q peak disappears. The presence of diffuse scattering agrees with previous discussion of the existence of SFs in LFS, and observations by Gruner et al. of diffuse scattering below $Q = 0.8$ Å^{-1}.[24] The behavior of the finite-Q peak in $LaFe_{11.8}Si_{1.2}$ mirrors observations made from latent heat measurements, where ΔS_{LH} decreases linearly as the tri-critical point was approached, indicating that it is directly related to the emergence of the first-order phase transition and the result of competing magnetic phases.

5. Experimental Section

Sample Preparation: Polycrystalline ingots of $LaFe_{13-x}Si_x$ ($x = 1.2$, 1.6) were prepared by arc melting constituent elements and annealing in argon at 1323 K (1596 °C) for 7 d. (Due to difficulties in the preparation of this alloy—a peritectic reaction that results in some α-Fe phase—only polycrystalline samples were available.)

Magnetization Measurements: Magnetometry was performed on a quantum design vibrating sample magnetometer at a field ramp rate of 0.5 T min^{-1}.

Inelastic Neutron Scattering (INS): INS measurements were performed on the MARI[27] and LET time of flight direct geometry spectrometers at the ISIS Neutron and Muon Source, UK. For these measurements, the sample was prepared in powder form by thermal cycling in liquid nitrogen, where the large associated magnetovolume transition results in fracturing of the ingot into ≈100–500 µm fragments. It was then contained in an aluminum foil packet sealed in a thin aluminum can with He exchange gas, which was cooled by an in-built He-flow cryostat in the case of high field measurements for $x = 1.2$ and a closed cycle refrigerator in the case of MARI and zero field LET measurements for $x = 1.6$. For the MARI measurements an incident energy of $E_i = 60$ meV was used, with the gadolinium chopper at 250 Hz, and $E_i = 150$ meV with the Gd chopper at 450 Hz. For the LET measurements a multi-chopper system was employed to simultaneously obtain data for incident energies of $E_i = 11.6$ (0.58), 3.6 (0.11), 1.73 (0.038), 1.02 (0.017), 0.67 (0.009) meV (in brackets is the full width half maximum resolution).[28]

X-Ray Diffraction: X-ray diffraction (XRD) patterns were obtained using a Bruker D2 Phaser with incident wavelength $\lambda = 1.54$ Å and a divergent slit width of 1 mm. The measurements were taken in θ/θ geometry with the diffracted beam optics composed of a 0.5 mm Ni monochromator and 2.5″ Soller slit followed by a 1D LYNXEYE detector with the detector opening set at 5.85°. Rietveld refinement was done using the FullProf Software.[29]

Calorimetry: AC microcalorimetry was obtained using the technique described in refs.[21, 30]. Selected samples of the order of µg were mounted on a 50 × 100 µm heater area of a commercial Xensor (TCG-3880) SiN membrane gauge that was adapted for thermal measurements. This technique is used in adiabatic conditions (where $\Delta T_{ac} = 0$) to determine heat expelled/absorbed due to a magnetic field driven first-order phase transition, ΔQ_{LH}, or under isothermal conditions (where $\Delta T_{ac} > 0$) to determine background changes in the heat capacity, ΔC_p. It has been shown elsewhere to be capable of separating the first order and continuous (second order) contributions to entropy change.[13,22,31–34] For clarification, throughout this manuscript, when referring to heat capacity, C_p, it is the background changes in the measured heat capacity in the absence of any latent heat that is presented, not the convolution of the two as is typically measured by bulk calorimetry methods.

Supporting Information

Supporting Information is available from the Wiley Online Library or from the author.

Acknowledgements

This work received funding from the European Community's 7th Framework Programme under grant agreement no. CP-FP 214864-2 and EPSRC grants EP/P002811/1 and EP/T034351/1. Experiments at the ISIS Neutron and Muon Source were supported by beamtime allocations RB1120323 and RB1320200 from the Science and Technology Facilities Council. The authors acknowledge Dr Keith Yendall and the Loughborough Materials Characterisation Centre for assistance and use of the facilities, and Dr David Voneshen and Dr Karl Sandeman for useful discussions. Supporting data from LET is available at https://doi.org/10.5286/ISIS.E.RB1320200; additional data presented here will be made available on FigShare under doi 10.17028/rd.lboro.13693525.

Conflict of Interest

The authors declare no conflict of interest.

Data Availability Statement

Supporting data from LET is available at https://doi.org/10.5286/ISIS.E.RB1320200; additional data presented here will be made available on FigShare under https://doi.org/10.17028/rd.lboro.13693525.

Keywords

intermetallics, itinerant, magnetocaloric, neutron scattering

Received: January 30, 2024
Revised: April 24, 2024
Published online:

[1] V. K. Pecharsky, K. A. Gschneidner Jr., *Adv. Mater.* **2001**, *13*, 683.
[2] J. Y. Law, L. M. Moreno-Ramírez, A. Díaz-Garcia, V. Franco, *J. Appl. Phys.* **2023**, *133*, 040903.
[3] A. M. Tishin, Y. I. Spichkin, V. I. Zverev, P. W. Egolf, *Int. J. Refrig.* **2016**, *68*, 177.
[4] A. Waske, *Nat. Energy* **2019**, *4*, 68.
[5] O. Gutfleisch, T. Gottschall, M. Fries, D. Benke, I. Radulov, K. P. Skokov, H. Wende, M. Gruner, M. Acet, P. Entel, M. Farle, *Philos. Trans. R. Soc., A* **2016**, *374*, 20150308.
[6] H. D. Nguyen, Z. Q. Ou, L. Caron, L. Zhang, D. T. C. Thanh, G. A. de Wijs, R. de Groot, K. H. J. Buschow, E. Brueck, *Adv. Energy Mater.* **2011**, *1*, 1154.

[7] N. M. Fortunato, A. Taubel, A. Marmodoro, L. Pfeuffer, I. Ophale, H. Ebert, O. Gutfleisch, H. Zhang, *Adv. Sci.* **2023**, *10*, 2206772.
[8] V. Franco, J. Y. Law, A. Conde, V. Brabander, D. Y. Karpenkov, I. Radulov, K. Skokov, O. Gutfleisch, *J. Phys. D: Appl. Phys.* **2017**, *50*, 414004.
[9] A. Fujita, K. Fukamichi, M. Yamada, T. Goto, *Phys. Rev. B* **2006**, *73*, 104420.
[10] A. Fujita, K. Fukamichi, *IEEE Trans. Magn.* **2005**, *41*, 3490.
[11] B. G. Shen, J. R. Sun, F. X. Hu, H. W. Zhang, Z. H. Cheng, *Adv. Mater.* **2009**, *21*, 4545.
[12] J. D. Moore, K. Morrison, K. G. Sandeman, M. Katter, L. F. Cohen, *Appl. Phys. Lett.* **2009**, *95*, 252504.
[13] K. Morrison, L. F. Cohen, *Metall. Mater. Trans. E* **2014**, *1*, 153.
[14] M. D. Kuz'min, M. Richter, *Phys. Rev. B* **2007**, *76*, 092401.
[15] A. Fujita, S. Fujieda, K. Fukamichi, *J. Magn. Magn. Mater.* **2004**, *272–276*, E629.
[16] K. Morrison, J. Lyubina, J. D. Moore, K. G. Sandeman, O. Gutfleisch, L. F. Cohen, A. D. Caplin, *Philos. Mag.* **2012**, *92*, 292.
[17] A. Fujita, *APL Mater.* **2016**, *4*, 064108.
[18] T. Faske, I. A. Radulov, M. Hoelzel, O. Gutfleisch, W. Donner, *J Phys.: Condens. Matter* **2020**, *32*, 115802.
[19] Z. Zhang, H. Zhou, R. Mole, C. Yu, Z. Zhang, X. Zhao, W. Ren, D. Yu, B. Li, F. Hu, B. Shen, Z. Zhang, *Phys. Rev. Mater.* **2021**, *5*, L071401.
[20] S. Fujieda, A. Fujita, K. Fukamichi, Y. Yamaguchi, K. Ohoyama, *J. Phys. Soc. Jpn.* **2008**, *77*, 074722.
[21] Y. Miyoshi, K. Morrison, J. D. Moore, A. D. Caplin, L. F. Cohen, *Rev. Sci. Instrum.* **2008**, *79*, 074901.
[22] K. Morrison, J. D. Moore, K. G. Sandeman, A. D. Caplin, L. F. Cohen, *Phys. Rev. B* **2009**, *79*, 134408.
[23] J. Landers, S. Salamon, W. Keune, M. E. Gruner, M. Krautz, J. Zhao, M. Y. Hu, T. S. Toellner, E. E. Alp, O. Gutfleisch, H. Wende, *Phys. Rev. B* **2018**, *98*, 024417.
[24] M. E. Gruner, W. Keune, J. Landers, S. Salamon, M. Krautz, J. Zhao, M. Y. Hu, T. Toellner, E. E. Alp, O. Gutfleisch, H. Wende, *Phys. Status Solidi B* **2018**, *255*, 1700465.
[25] S. Bao-Gen, H. Feng-Xia, D. Qiao-Yan, S. Ji-Rong, *Chin. Phys. B* **2013**, *22*, 017502.
[26] F. Long, Y. Song, J. Chen, *Microstructures* **2024**, *4*, 2024011.
[27] M. D. Le, T. Guidi, R. Bewley, J. R. Stewart, E. M. Schooneveld, D. Raspino, D. E. Pooley, J. Boxall, K. F. Gascoyne, N. J. Rhodes, S. R. Moorby, D. J. Templeman, L. C. Afford, S. P. Waller, D. Zacek, R. C. R. Shaw, *Nucl. Instrum. Methods Phys. Res. A* **2023**, *1056*, 168646.
[28] R. I. Bewley, J. W. Taylor, S. M. Bennington, *Nucl. Instrum. Methods Phys.* **2011**, *637*, 128.
[29] J. Rodriguez-Carvajal, *Phys. B* **1993**, *192*, 55.
[30] A. A. Minakov, S. B. Roy, Y. V. Bugoslavsky, L. F. Cohen, *Rev. Sci. Instrum.* **2005**, *76*, 043906.
[31] K. Morrison, J. Lyubina, J. D. Moore, A. D. Caplin, K. G. Sandeman, O. Gutfleisch, L. F. Cohen, *J. Phys. D: Appl. Phys.* **2010**, *43*, 132001.
[32] K. Morrison, M. Bratko, J. Turcaud, A. Berenov, A. D. Caplin, L. F. Cohen, *Rev. Sci. Instrum.* **2012**, *83*, 033901.
[33] K. Morrison, A. Dupas, Y. Mudryk, V. K. Pecharsky, K. A. Gschneidner, A. D. Caplin, L. F. Cohen, *Phys. Rev. B* **2013**, *87*, 134421.
[34] K. Morrison, S. M. Podgornykh, Y. V. Shcherbakova, A. D. Caplin, L. F. Cohen, *Phys. Rev. B* **2011**, *83*, 144415.